JOURNAL OF PROPULSION AND POWER
Vol. 21, No. 5, September–October 2005

Side Force Reduction of Cone–Cylinder Using Microballoon Array Actuator

Tzong-Shyng Leu,* Jeng-Ren Chang,† and Pong-Jeu Lu‡
National Cheng Kung University, Tainan 701, Taiwan, Republic of China

The reduction of side force acting on a cone–cylinder slender body using a microballoon array actuator is examined. This microballoon array actuator can be inflated to a height of approximately 1.2 mm on the curve surfaces of the slender body. Experimental results indicate that side forces can be significantly reduced by inflating actuators near the weak and strong separated vortex structures. The mechanism of side force reduction has been investigated via both hot-wire and surface pressure measurements. Interestingly, unlike the conventional methods of changing the vortices from asymmetric to symmetric pairing for side force reduction, a microballoon array actuator makes vortices more asymmetric. It was found that two mechanisms can characterize the reduction of side force. The first mechanism involves that the weak side vortex lifts off prematurely because the microballoon actuation replaces the vortex pair structures with a more asymmetrically positioned pattern, enabling the formation of a new (third) vortex in the near-wall region. The second mechanism involves the strength of the newly generated (third) vortex being able to be effectively controlled via the microballoon actuation. Microballoon actuators can effectively alter the evolution of the new (third) near-wall vortex structure.

Nomenclature

A = cylinder cross-sectional area
C_n = normal force coefficient, $N/q_\infty A$
C_p = pressure coefficient, $(p - p_\infty)/q_\infty$
C_s = total side force coefficient, $S/q_\infty A$
$C_{s,X/D}$ = sectional side fore coefficient at X/D,

$$-\frac{1}{D}\int_0^{2\pi} C_P(\sin\theta) r \,\mathrm{d}\theta$$

D = cylinder diameter
L = body length
N = normal force
p = surface static pressure
p_∞ = freestream static pressure
q_∞ = freestream dynamic pressure, $\frac{1}{2}\rho U_\infty^2$
Re = Reynolds number, $U_\infty D/\nu$
S = side force, defined positive in positive Y-axis direction
U, V, W = velocities in X, Y, Z directions, respectively
U_∞ = freestream velocity
X, Y, Z = coordinate system fixed with test model, as shown in Fig. 1
ν = dynamic viscosity of air
φ_a = microballoon actuator position
φ_p = circumferential location of pressure orifices
φ_r = roll angle
ω_x = nondimensional streamwise vorticity, $(\partial W/\partial Y - \partial V \partial Z)/(U_\infty/D)$

I. Introduction

SIDE force occurrence on slender bodies of revolution at medium to high angle of attack [(AOA) > 300 deg] has long been observed. Flowfield features and characteristics for a slender body at high AOA have received considerable attention.[1–4] These investigations brought useful information in understanding the behavior of a slender body at high AOA. This information could be used to improve the design of high-performance aircraft and guided missiles. These studies demonstrate that AOA is the key flowfield parameter. For a slender body at moderate AOA ($10 < \mathrm{AOA} < 30$ deg), the flow separating from the body rolls up into a pair of symmetric vortices. These symmetric vortices may become asymmetric when the AOA exceeds some critical value. Significant side force results from the appearance of these two asymmetric vortices. The magnitude of this side force can equal that of the normal force acting on the slender body, which frequently causes an aircraft to spin or a missile to tumble in situations where these effects are not thoroughly considered as part of the control system design.

A peculiar phenomenon is associated with high-AOA slender-body flow, namely, a geometrically symmetrical body may develop asymmetric airloads when rotated around its axis of revolution. Accordingly, roll angle was introduced as another important parameter, in addition to AOA, for characterizing the slender-body flow. With regard to the roll angle effect, a number of researchers have found that side force depended heavily on roll angle.[5,6] As AOA exceeded the vortex onset angle that generates side force, the variation of side force with respect to the roll angle altered from a continuous distribution to a square waveformlike distribution.[5] Zilliac et al.[5] further examined the trends of side force variation vs nose roll angle. Tiny imperfections, even as small as the dust particles (approximately 3-μm diameter) incidentally coating the nose of the model, were found to change the direction and phase of the side force distribution in response to the roll angle change. The finding by Zilliac et al.[5] implies that the leading-edge vortex genesis and subsequent growth are highly sensitive to small imperfections of the nose tip. In addition to the AOA and the roll angle, side force is also sensitive to other parameters, including nose fineness ratio, nose bluntness, nose geometry, Reynolds number, body slenderness, surface roughness, freestream turbulence, and so on.[6–10] However, for simplicity, this study only considers AOA and roll angle.

Aerodynamic control of a slender body at moderate to high AOA flow is important for combat air vehicles. Recently, numerous

---

Received 7 September 2004; revision received 1 March 2005; accepted for publication 1 March 2005.

*Assistant Professor, Department of Aeronautics and Astronautics, Number 1 University Road; tsleu@mail.ncku.edu.tw.

†Ph.D. Candidate, Department of Aeronautics and Astronautics, Number 1 University Road.

‡Professor, Department of Aeronautics and Astronautics, Number 1 University Road.

techniques have been developed for controlling forebody vortices. These control methods can be divided into two categories, namely, passive and active methods. Passive control methods are relatively simple and require no auxiliary power or control loop. However, active control methods require a sensor and feedback loop system to sense the current states and require energy expenditure to actively facilitate the control actuation.

With regard to the passive control methods, one such method[11] involved a pair of helical trips that were used to force nonuniform crossflow separation from the forebody to disrupt the formation of concentrated leeside vortices. Experiments demonstrated that the helical trip device can effectively reduce the side force. Clark and Peoples[12] installed small winglets on the forebody to alter the wake flowfield. The experimental results demonstrated that the proposed device could markedly reduce yawing moments. Asghar et al.[13] investigated side force control by adding a leeside fin to a circular cone. Flow visualization tests showed that the fin can generally suppress the asymmetric vortices.

Regarding active control methods, Moskovitz et al.[14] used a rotating forebody tip that varies in cross-sectional shape from a circle at its base to an ellipse at its apex. Variation of side force with roll angle is found quite obvious, and side force can be controlled by adjusting the tip roll angle. Fidler[15] controlled the asymmetric vortex on a slender body at high AOA by rotating the nose. Numerous researchers[16–19] investigated the blowing methods of controlling the side force and yawing moment of aircraft and missiles. The experimental results showed that a small amount of blowing momentum is sufficient to produce a significant change in the side force and yaw moment. Forebody vortex flow can also be controlled by the movable strakes.[20,21] The experimental results showed that the side force of the model could be considerably changed as strakes were actuated at different azimuth positions. However, it was also found that excessively large nose strakes may induce pitching instability. The side-jet control method[22,23] has been employed for controlling missile attitude because of its rapid burning rate, which generates instant control forces. Furthermore, the side-jet force can be amplified by the interaction between the side jet and the external flow. To summarize, the effectiveness of all of the previously mentioned control methods stems from producing aerodynamic forces and moments by influencing the characteristic vortex dynamics structure over the slender forebody region.

Recently, microelectromechanical-system technology has developed rapidly because of its numerous advantages, such as low cost, fast response, high sensitivity, small volume, light weight, redundancy, and so on. Grosjean et al.[24] conducted the experiment of F-15 fighter aerodynamic control by using microballoon actuators packaged on the leading edge of the wing. Their experimental results demonstrated that the rolling moment could be influenced once microballoon actuators were actuated. Lee et al.[25] installed micromagnetic actuators on the leading edge of a delta-wing airplane. Following actuation, the rolling, pitching, and yawing moments on delta-wing aircraft changed markedly. Huang et al.[26] controlled an unmanned aerial vehicle sized aircraft using the so-called M^3 system that combined the microactuators, microsensors and microelectronics in a single device. These examples show that microactuators can serve as an excellent tool for aerodynamic control despite their small size. Provided microactuators are actuated at the sensitive places of the vehicle, small disturbances caused by microactuators can be amplified via the instability mechanism of the flowfield, creating macroscaled control forces for maneuvering the flying vehicles.

Previous studies found that the most effective way of controlling the side force of a slender body was to interfere with the initial vortex generation position near the forebody apex. Creating a small disturbance near the apex can significantly change the features of the vortical flowfield over a slender body at a high AOA. Moreover, the effectiveness and mechanism of microarray actuators have not been completely studied and are not well understood for slender-body flow. Based on this, this study investigates the control effects of the flexible microballoon array actuator on the aerodynamic characteristics associated with a cone–cylinder. The most sensitive region of actuation over this cone–cylinder slender body was also searched for. Nevertheless, the tiny space imposes practical difficulties for installing an active actuator in the apex region. As a result, the best possible location for control implementation is the cone surface, where flow is still highly susceptible to disturbances.

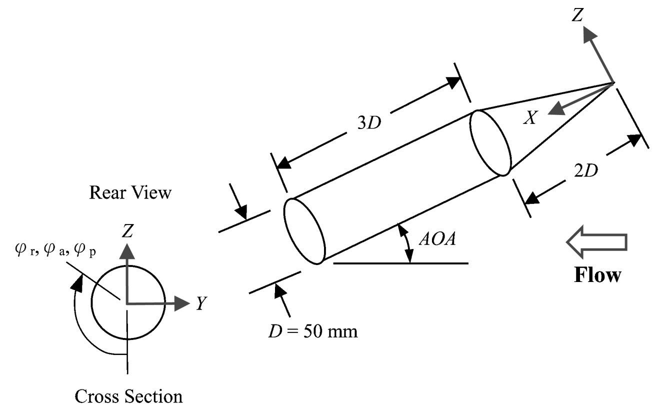

Fig. 1 Schematic of coordinate systems.

II. Experimental Setup

Experiments were conducted in an open-type low-speed wind tunnel. The test section is a circular tube 50 cm in diameter and 140 cm in length. The flow speed at the test section ranges from 2.0 to 35.0 m/s, and the turbulence intensity is less than 0.5%.

A body-fixed coordinate system (X, Y, Z) is used to describe the flowfield measurements and the physical quantities to be discussed. This coordinate system is illustrated in Fig. 1. The X axis points in the downstream direction along the body axis of revolution. The Y axis directs the starboard direction, with the Z axis defined using a right-hand rule. Angular positions such as roll angle φ_r, actuation angle φ_a, and pressure orifice angle φ_p are defined positive in a clockwise sense and measured from the windward stagnation point on the plane $Y = 0$.

The experimental model is a cone–cylinder slender body, and the diameter of the cylinder D is 50 mm. The cone has a fineness ratio of two and the cylinder length is three times of its diameter. An annular recess was machined 60 mm in length along the cone surface, from $X/D = 0.84$ to 2, and 0.8 mm in depth over the cone region of the model. It is generally agreed that the slender-body vortical flow is most sensitive to the conditions near the tip region. Because the actuators are placed as close as possible near the tip of the cone, the control effectiveness should be more significant. Because of the limited space and the difficulties of the package near the apex of the cone, it was chosen in the current study to place the actuators spread from $X/D = 0.84$ to 2 over the cone section. A fan-shaped flexible microballoon array actuator can be flush mounted on the curved surface of the cone section. Also, the pressure orifices are drilled annularly around the $X/D = 2.4$ and 3.6 stations, respectively, both measured from the cone apex. The pressure orifices have an interval of 10-deg separation among one another. Figures 2a and 2b show photographs of the cone–cylinder model and the wind-tunnel experimental setup.

Surface pressure and overall aerodynamic forces of the cone–cylinder are measured using a pressure transducer and load cell, respectively. The velocity measurement is measured using, respectively, the single-type and X-type hot wires. The hot wire is mounted on a three-dimensional traversing mechanism that is controlled by a microprocessor-based computer. Velocity flowfield measurement, however, will be utilized to show the vortex pair structure variation caused by the actuation of the microballoon actuators.

III. Microfabrication of Flexible Microballoon Actuator

Grosjean et al.[24] first used a microballoon actuator for aerodynamic control in 1998. They performed the experiment on a fighter F-15 aerodynamic control by using microballoon actuators

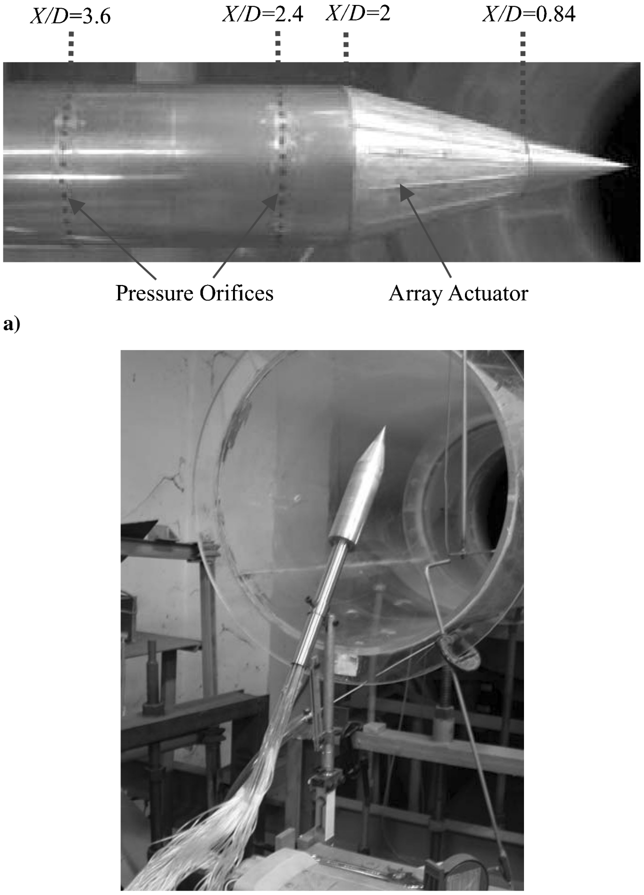

Fig. 2 Photographs of a) cone–cylinder model and b) wind-tunnel experimetnal setup.

packaged on the wing surface. Their experimental results indicated that the rolling moment could be effectively influenced once microballoon actuators are actuated at critical locations on the leading edge of the wing. Because the actuators used by Grosjean et al.[24] are rigid substrates, the original curved geometry of the leading edge of the wing surface has to be reshaped when the actuators are installed. In the present study, a flexible microballoon array actuator was manufactured using a newly designed micromolding technology.[27] In so doing, the microballoon array actuator can be packaged on any curve surface of the cone–cylinder slender body without surface profile modification. All parts of the actuator are made from polydimethylsiloxane (PDMS).[28] The mother mold is a fan-shaped mold milled by the use of precision machining. It includes six actuator membranes that are molded in a fan-shaped distribution. The membrane area is 50×2 mm in length and width, and the base depth of the flexible microballoon actuators is approximately 400 μm. Figure 3 shows the schematic of the flexible microballoon array actuator.

The fabrication processes of the flexible microballoon actuators are described as follows. An excessive amount of PDMS is injected into the mother mold first. Then, the membrane thickness is controlled by the rotational speed of the spin coater. The centrifugal force, which is governed by the rotational speed, can fling away the excessive PDMS. Then, the mother mold is put on a horizontal plane for approximately 10 min to let the PDMS settle. The mother mold is finally placed on a heated plate, set at a baking temperature of 100°C for 20 min for shape forming. The test results show that the membrane thickness possesses excellent uniformity and can be controlled precisely.

In this study, the flexible microballoon actuator is actuated by using external high-pressure source. For all wind-tunnel experiments in this study, the pressure source is fixed at 11 psig ($\sim$180000 N/m^2), and the actuator membrane can be inflated to about 1.2 mm in height at this pressure setting.

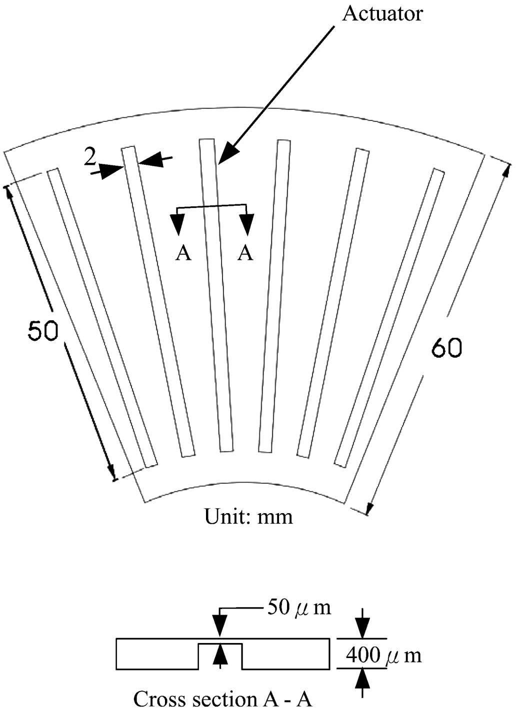

Fig. 3 Schematic of cone-shaped microballoon array actuator.

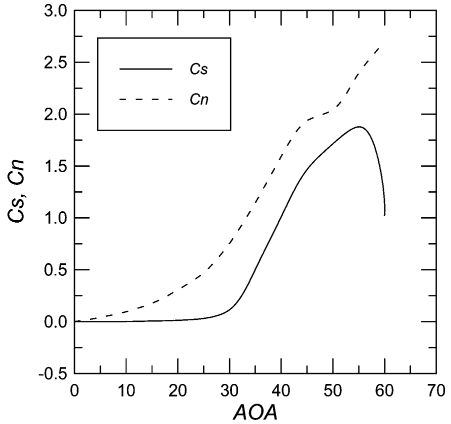

Fig. 4 Distributions of side force coefficient C_s and normal force coefficient C_n of cone–cylinder slender body at different AOA, no microballoon actuation and roll angle fixed at $\varphi_r = 100$ deg.

IV. Aerodynamic Characteristics of Cone–Cylinder Slender-Body Flow

The present experiments were conducted in an open-type low-speed wind tunnel. The operational flow speed at the test section can range from 2.0 to 35.0 m/s. In this paper, the results are shown for a freestream velocity of $U_\infty = 20$ m/s and a Reynolds number, defined as $Re = \rho U_\infty D/\mu$, of 6.7×10^4. Other experiments have also been investigated for different Reynolds number ranges, $Re = 6.7 \times 10^3 \sim 1.2 \times 10^5$, in this wind tunnel. The results are qualitatively similar to those of the experiment with $Re = 6.7 \times 10^4$. The side force S, defined positive in the Y direction (starboard direction as viewed from downstream), was measured by the use of a load cell.

Before investigating the effect of the microballoon array actuator on the slender-body aerodynamics, the experiments were first conducted to study the high-AOA aerodynamic characteristics of the cone–cylinder slender body with no microballoon control actuation. Figure 4 shows the control-free normal force coefficient C_n and the side force coefficient C_s variations with the AOA changing from 0 to 60 deg and the roll angle fixed at $\varphi_r = 100$ deg. This shows that the side force increases rapidly when the AOA exceeds 30 deg. The side force reaches its maximum within the AOA range between 50 and 55 deg. Once the AOA increases beyond 55 deg, the side force decreases dramatically. When the crossflow characteristics of the cone–cylinder slender body were analyzed, it was found that symmetric vortex pairs rolled up on the leeward side of the forebody for the low-to-medium AOA range AOA $\leq$30 deg. The symmetry of the vortex pair makes the side force in this AOA range negligible. When AOA further increases beyond 30 deg, the original symmetric vortex pairs become asymmetric and the side force starts to appear. The side force approaches its maximum as AOA reaches about 50 ~ 55 deg. If the AOA is further increased, the side force drops abruptly, and the flow exhibits unsteady wakelike vortex shedding, which is similar to the flow over a vertical circular cylinder.

As asymmetric vortex pair or side force prevails, the surface pressure distribution becomes asymmetric also. The vortex-induced surface pressure variations are unequally distributed over the two sides of the leeward region, with one side variation much stronger than the other. In this study, for the sake of convenience, the vortex side was named the strong vortex side, for the much stronger vortex-induced surface pressure variation, and the other side was named the weak vortex side. Because of the asymmetric flow separation and the hydrodynamic instability of the symmetric vortices, the strong side vortex is located closer to the leeward surface of the slender body. The strong side vortex may generate stronger negative pressure (suction force) on the slender body. Figure 4 also shows that the normal force increases with AOA. Moreover, the variation of normal force is found to be more regular and monotonic in trend than that of the side force.

In addition to the AOA influence, side force also varies with roll angle φ_r even when microballoon actuators are not actuated. Figure 5 shows the variation of side force with respect to the roll angle when AOA is increased from 40 to 55 deg. There exists an oscillatory distribution of the side force as roll angle changes. It is observed that side force variation with roll angle is characterized by a trend of low to moderate, asymmetric wavy distribution when the AOA is set at AOA = 40 and 45 deg, as shown in Figs. 5a and 5b. As a higher AOA is attained between 50 and 55 deg, the side force exhibits a square-wavelike pattern and periodically changes its direction between positive and negative values as roll angle varies, as shown in Figs. 5c and 5d.

For the cases illustrated in Figs. 5c and 5d, the variations of side force with roll angles and the associated vortical structures can be divided into three types. In the first type, net side force is negative for roll angle in the ranges of $0 < \varphi_r < 70$ deg and $170 < \varphi_r < 220$ deg. In the second type, for roll angles residing in the regions of $90 < \varphi_r < 150$ deg and $240 < \varphi_r < 310$ deg, the side force is positive. For these two types, flowfield is characterized by a stable asymmetric vortex pair, and the induced side force is either positive or negative depending on which side the strong vortex is located. In the third type, it is found in the experiments that the vortical structures exhibit unsteadiness, causing the model vibrate for roll angles in the regions of $70 < \varphi_r < 90$ deg, $150 < \varphi_r < 170$ deg, and $220 < \varphi_r < 240$ deg, where side force switches intermittently from negative (or positive) to positive (or negative) values. When taking a long-time average of the third type of side forces, it is found that the fluctuating side force may result in a nearly zero mean in these unsteady flow regions. Variation of the normal force with roll angle for AOA fixed at 50 deg is also shown in Fig. 6. It is observed that the variation of normal force with roll angle is significantly smaller than that of the side force. Therefore, the emphasis of the present study will focus on the side force control for either the first (negative) or the second (positive) side force type. For these two types, flowfield is characterized by a stable asymmetric vortex pair. Hot-wire, pressure, and force sensor signals show basically steady trends with small fluctuations superimposed. The time-averaged measurements can, therefore, represent the characteristics of the vortical flowfield studied.

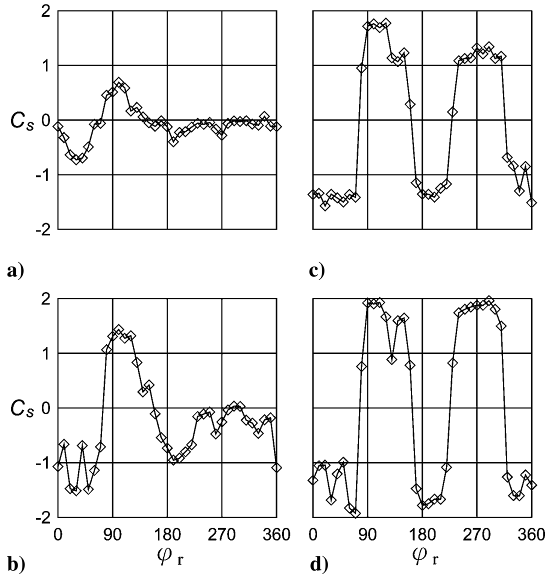

Fig. 5 Variations of side force coefficient C_s at different roll angles φ_r when AOA is a) 40, b) 45, c) 50, and d) 55 deg.

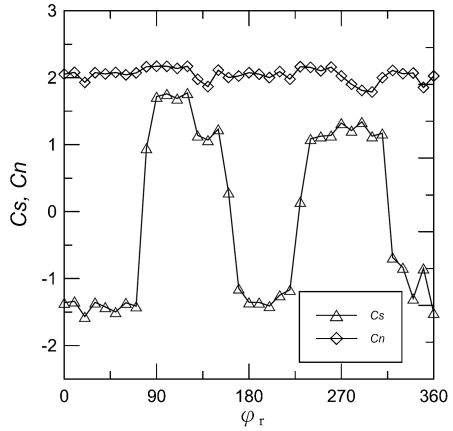

Fig. 6 Variations of side force coefficient C_s and normal force coefficient C_n of cone–cylinder slender body at different roll angles (AOA = 50 deg).

V. Microballoon Controlled Cone–Cylinder Slender-Body Flow

A. Single Actuator Control

The aerodynamic characteristics of the control-free cone–cylinder slender-body flow have been investigated in the preceding section. They indicate that side force generated for the cone–cylinder slender body is extremely sensitive to the AOA and the roll angles as well. The present work further explores the microballoon controlled aerodynamics of the cone–cylinder slender body at high AOA. In this section, single actuation is first investigated. Figure 7 shows the variation of the side force coefficient C_s when one microballoon actuator is actuated at different actuation angles φ_a. Two effective actuation angle regions have been found based on the side force direction preference before control actuation. For those side forces that are positive before actuation ($\varphi_r = 100$, 120, and 290 deg, shown in Fig. 5d), the side force can be effectively alleviated when the actuator is actuated in the region from $\varphi_a = 50$ to 90 deg. On the other hand, for those side forces that are negative before actuation ($\varphi_r = 60$, 190, and 200 deg, shown in Fig. 5d), the side force can be reduced significantly as a single actuator is actuated in the region from $\varphi_a = 270$ to 310 deg. Recall that when initial side force is positive (or negative) before actuation, the 0 ~ 180 deg (or 180 ~ 360 deg) half-side of the cone–cylinder slender body corresponds to the weak vortex side defined earlier. Moreover, the effective actuation angle range of $50 < \varphi_a < 90$ deg for the positive side force case is the mirror image of the effective region of $270 < \varphi_a < 310$ deg with respect to the dividing symmetry plane for the negative side force case.

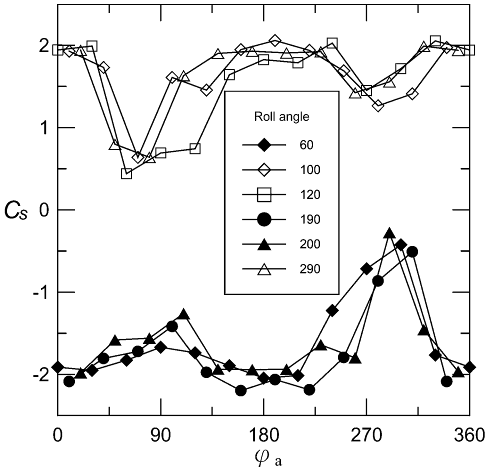

Fig. 7 Variations of side force coefficient of cone–cylinder slender body with single actuator forcing at different actuation angles φ_a for various roll angles φ_r (AOA = 55 deg).

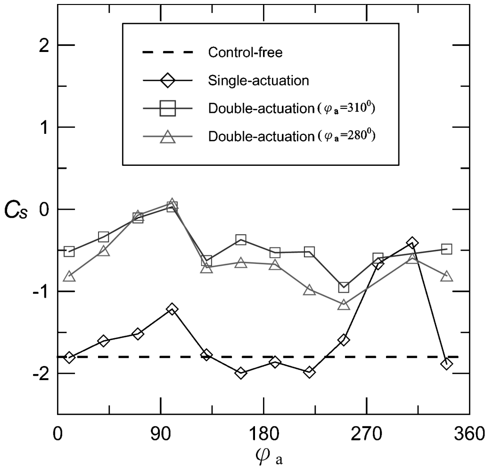

Fig. 8 Side force coefficient C_s of cone–cylinder slender body for case of AOA = 55 deg and roll angle $\varphi_r = 190$ deg.

For both cases, effective controls all occur at an angle range within $50 < |\varphi_a| < 90$ deg, as measured from the windward stagnation line toward the weak vortex side. The same experiments were also conducted for other AOA at 50, 45, and 40 deg, respectively. The results indicate that the preceding effective actuation angle works equally well and shows no dependence on these AOA. A very useful conclusion can be drawn from these experimental observations; namely, the side force can be effectively alleviated when the microballoon actuator is located on the weak vortex side, within an actuation angle range of $50 \sim 90$ deg measured from the windward stagnation line.

B. Multi-Actuator Control

The results shown in the preceding section indicate that a single actuator can significantly alleviate the side force of the cone–cylinder slender body when the actuator is forced within an appropriate angle range over the weak vortex side. Follow-up experiments further explored the flow controlled simultaneously by two actuators. Figure 8 shows the results when the AOA = 55 deg and the roll angle at $\varphi_r = 190$ deg. The diamond symbols in Fig. 8 represent the results that side force reduction can be significantly achieved when a single actuator control is enforced within $280 < \varphi_a < 310$ deg. The experiments with double actuations are then conducted for one actuation employed at either $\varphi_a = 280$ or 310 deg, combined with the other actuator actuated at different actuation angles within $0 < \varphi_a < 360$ deg. Figure 8 shows that the side force can be further reduced to nearly zero when one actuator working at the effective actuation angle range over the weak vortex side ($\varphi_a = 280$ or 310 deg) is augmented by the other side force actuated simultaneously at $\varphi_a = 100$ deg.

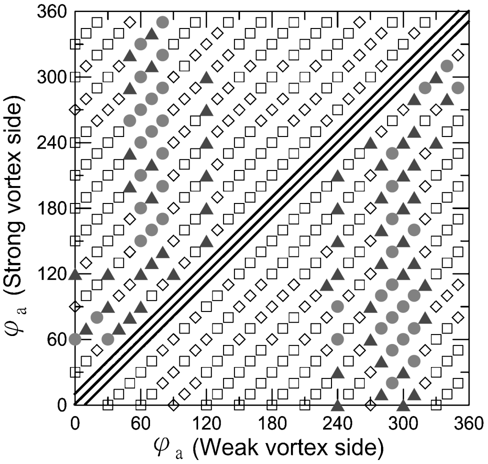

Fig. 9 Distribution of side force magnitudes when two actuators are employed (AOA = 55 deg), lower and upper triangular portions are for cases with side force being originally negative (φ_r = 60, 190, and 200 deg) and originally positive (φ_r = 100, 120, and 290 deg), respectively: ●, $|C_s| < 0.5$; ▲, $0.5 < |C_s| < 1$; ◇, $1 < |C_s| < 1.5$; and □, $|C_s| > 1.5$.

Extensive studies have been performed to examine the multi-actuation effectiveness. Figure 9 illustrates the results and shows the distributions of side force when any combinations of two actuators are employed for a cone–cylinder body at AOA = 55 deg. The absolute values of the control-free side force coefficients fall between 1.7 and 2.0. For cases with side force being originally negative ($\varphi_r = 60$, 190, and 200 deg) or originally positive ($\varphi_r = 100$, 120, and 290 deg), the magnitudes of side force coefficient $|C_s|$, when control was activated, are found to be distributed in the lower and upper triangular portions of Fig. 9, respectively. These side force amplitudes are classified into four levels, namely, filled circular symbols for $|C_s| < 0.5$, filled triangular symbols for $0.5 < |C_s| < 1.0$, hollow diamond symbols for $1.0 < |C_s| < 1.5$, and hollow square symbols for $|C_s| > 1.5$. The lower triangular portion of Fig. 9 represents the results for the initially negative side force flows whose corresponding weak vortex sides are located in the region of $\varphi_a = 180$–360 deg. For those cases, most of the side force can be effectively alleviated when one actuator is placed in the region of $270 \sim 310$ deg (the weak vortex side) and the other located in the region of $60 \sim 110$ deg (the strong vortex side). Similarly, the data in the upper triangular portion of Fig. 9 describe the results associated with originally positive side force cases having their corresponding weak vortex side located in the region of 0–180 deg. For these flowfields, side forces can be effectively reduced when actuators are located in the regions of $50 \sim 90$ deg (the weak vortex side) and $250 \sim 300$ deg (the strong vortex side), respectively. Both results can be summarized in a simple rule that states that the side force can be effectively reduced using one actuator located in the region of $50 \sim 90$ deg (weak vortex side) and the other in the region of $60 \sim 110$ deg (strong vortex side), measured oppositely from the stagnation line on the windward side.

The experiments also included studies of the induced normal force when two actuators located in the regions of $50 \sim 90$ deg and $250 \sim 300$ deg are employed. Figure 10 shows a typical normal force for AOA varying from 0 to 60 deg when the roll angle is fixed at $\varphi_r = 100$ deg. It is seen that, in the high-AOA range, the normal force could be slightly enhanced when two actuators located at $\varphi_a = 70$ and 280 deg were turned on. Figure 11, however, shows the side force annihilation due to this flow control using two balloon actuators. Figures 10 and 11 together show that, at high AOA, lift can be maintained or enhanced, whereas the undesirable side force is greatly eliminated using the present multi-actuation method. For other roll angles at different angles of attack, the experimental results also indicate that the side force can be reduced with the same trends as shown in Fig. 11. Physically, the present flow control method adjusts the asymmetry of the leeward side vortical structures. However,

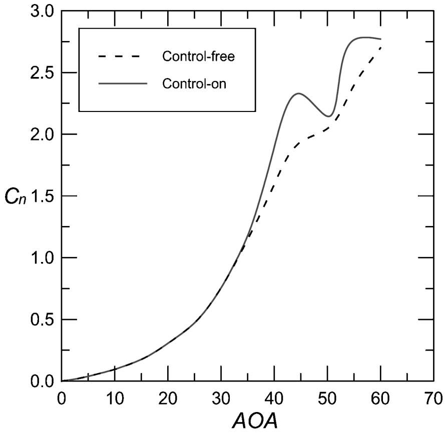

Fig. 10 Comparison of normal forces generated at different AOA ($\varphi_r = 100$ deg), actuators located at $\varphi_a = 70$ and 280 deg.

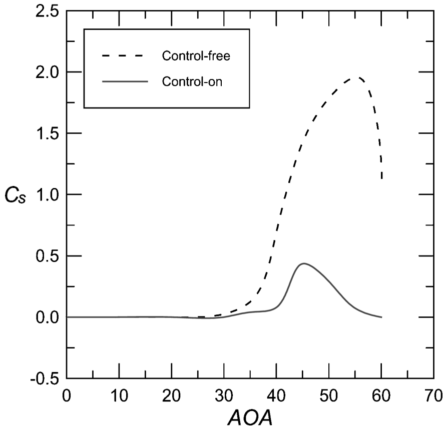

Fig. 11 Comparison of side forces generated at different AOA ($\varphi_r = 100$ deg), actuators located at $\varphi_a = 70$ and 280 deg.

the overall coherence of the vortex formation mechanism is not sacrificed, resulting in a strong suction effect that is maintained on the leeward side and produces the vortex lift required.

VI. Mechanism of Side Force Reduction Using Microballoon Array Actuator

The preceding force measurement experiments conjecture an enhanced vortical structure that dwells on the leeward side as the balloon actuators were activated. To determine more precisely how this control-induced vortical structure is, it is necessary to examine flowfield measurements to elaborate on the physical mechanism involved.

A. Flowfield Velocity Measurement

To understand the detailed mechanisms of side force reduction with microballoon actuation calls for three-dimensional velocity measurements. An X-type hot wire has been used twice to measure the velocity data sets of (U, V) and (U, W) and was then converted into a three-dimensional velocity (U, V, W) field. Figures 12 and 13 illustrate the cross-sectional (V, W) velocity vector plots obtained at $X/D = 3.6$ for the slender body without and with control actuation. These velocity vectors are constructed by taking the long-time average of the measured data. Figures 14 and 15, however, show the constant nondimensional streamwise vorticity ω_x contours calculated from those velocity vectors, respectively.

The vortex pair structures are clearly identified in Figs. 12 and 13. Note that one vortex is situated close to the body surface on the right-side and the other away from the body surface on the left-hand side. This asymmetric vortex pair induces a strong positive side force. In Fig. 12, the left- and right-side vortex core positions $(Y/D, Z/D)$ appear to be roughly at $(-0.5, 1.8)$ and $(0.4, 0.45)$, which coincides with the locations of the maximum streamwise vorticity seen in Fig. 14. Note that in Fig. 13 the vortex cores move to new positions $(Y/D, Z/D)$ at $(-.0.4, 2.3)$ and $(0.5, 0.75)$ when microballoons are actuated, respectively, at $\varphi_a = 70$ and 250 deg. Figure 13 shows that the vortex on the left side (weak vortex side) migrates upward to a position further away from the cylinder. Note that instead of changing vortex structures from being asymmetric to symmetric for side force reduction, which the conventional control methods adopted, microballoon array actuation causes vortex pair structures become even more asymmetric. As noted in Figs. 14 and 15, a third high vorticity-concentrated region is formed over the near-wall region of the left side (weak vortex side). Figure 14 illustrates that the original third vortex was loosely formed at the near-wall position $Y/D = -0.7$, $Z/D = 0.7$ before the control actuation. When control is turned on, this third vorticity-concentrated region is strengthened into a clear vortex structure appearing at $Y/D = -0.5$, $Z/D = 0.45$, as shown in Fig. 15.

Collecting seven sectional velocity measurements together, one can derive a depiction of the weak-side vortex core and the third vortex core trajectories developed from the cone apex. Figure 16 shows

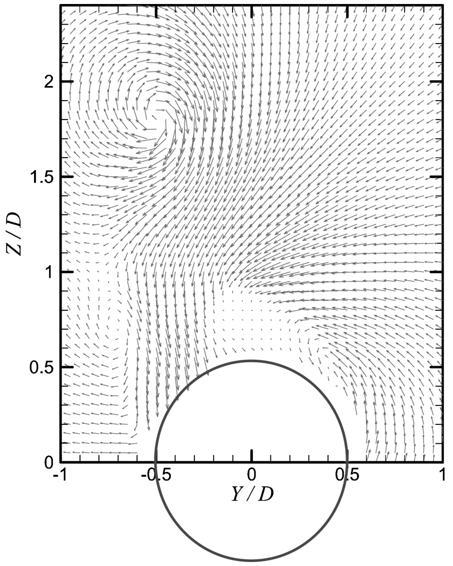

Fig. 12 Sectional velocity vector distribution: $X/D = 3.6$, AOA = 50 deg, $\varphi_r = 100$ deg, and control free.

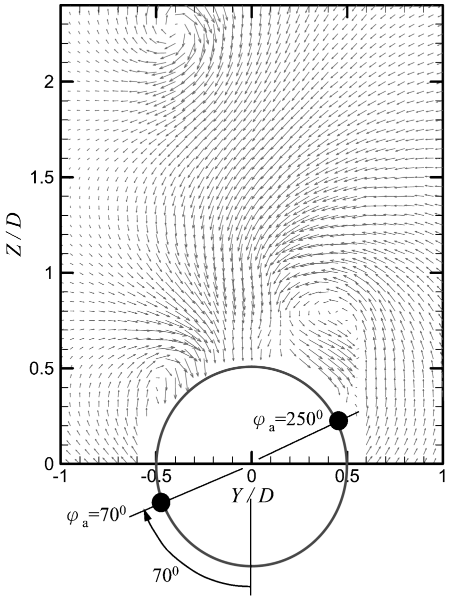

Fig. 13 Sectional velocity vector distribution: $X/D = 3.6$, AOA = 50 deg, $\varphi_r = 100$ deg, double actuation, and $\varphi_a = 70$ and 250 deg.

the trajectory of the weak-side vortex cores, which initially stay close to the model surface above the cone section, and then experience a liftoff at downstream location $X/D = 2.4$ above the cylinder section, caused by the formation of a third vortex structure developed inboard around the leeward surface. Luo et al.[6] conducted similar flow visualization experiments using an ogive–cylinder model held at AOA = 50 deg. Their investigation found that the weak-side vortex lifts off earlier than the strong-side vortex, and at the same time a third near-wall vortex is formed at the weak vortex side. In Fig. 16, similarly, it is found that the weak-side vortex, when forced by microballoon actuation, lifts off earlier around location $X/D = 1.6$ as compared to the one without control actuation. The enhanced new (third) vortex also shows premature liftoff in the near-wall region as microballoon actuation is employed.

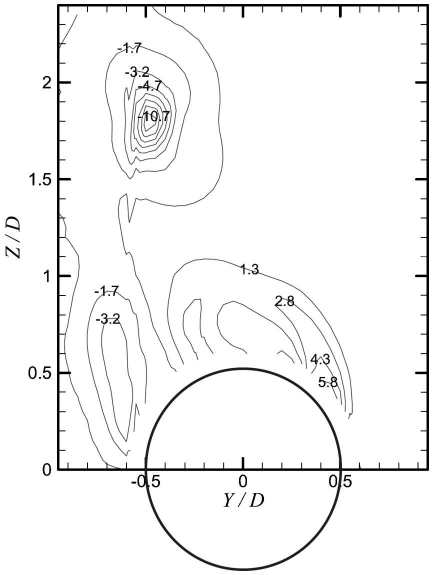

Fig. 14 Nondimensional streamwise vorticity ω_x: $X/D = 3.6$, AOA = 50 deg, $\varphi_r = 100$ deg, and control free.

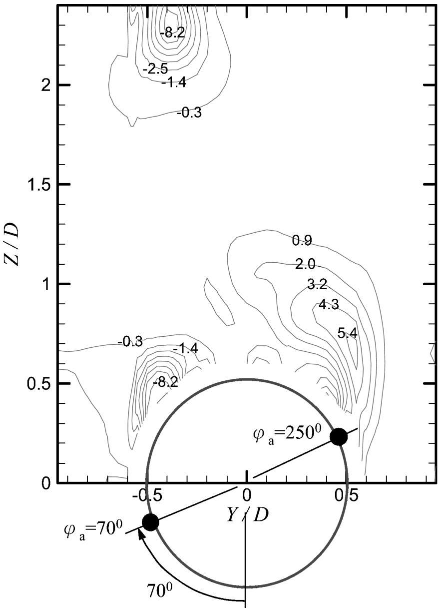

Fig. 15 Nondimensional streamwise vorticity ω_x: $X/D = 3.6$, AOA = 50 deg, and $\varphi_r = 100$ deg, double actuation, and $\varphi_a = 70$ and 250 deg.

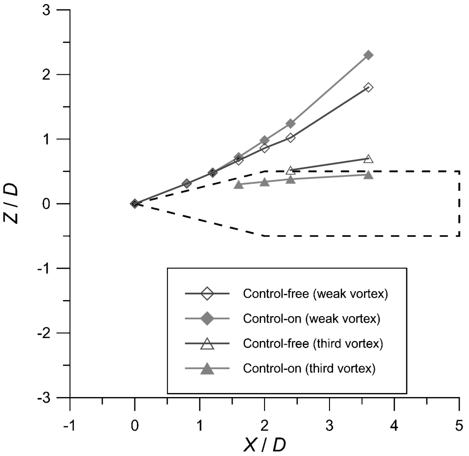

Fig. 16 Side view of vortex core trajectories developed from cone apex: AOA = 50 deg, $\varphi_r = 100$ deg, double actuation, $\varphi_a = 70$ and 250 deg, control-free side force $C_s = 1.79$, and control-on side force $C_s = 0.29$.

B. Sectional Side Force Measurement

Figures 17 and 18 show the surface pressure distributions obtained on the cross sections $X/D = 2.4$ and 3.6 for the cone–cylinder held at AOA = 55 deg and $\varphi_r = 70$ deg. In Figs. 17 and 18, the surface distributions associated, respectively, with control-free, single actuation at $\varphi_a = 280$ deg and double actuation at $\varphi_a = 280$ and 100 deg are illustrated. Figures 17 and 18 show that the body surface experiences greater suction (negative) pressure on the left side (strong vortex) side than on the right side (weak vortex) side before microballoon actuation. The asymmetric distributions of the surface pressures between $0 \sim 180$ deg and $180 \sim 360$ deg cause side force formation in the control-free flowfields. For single- and multi-actuation cases, the degree of asymmetry at cross section $X/D = 2.4$ (Fig. 17) is significantly decreased. By integrating surface pressure distributions, one can calculate the sectional side force (side force per unit span) along the cylinder. At section $X/D = 2.4$, the sectional side force is alleviated after control actuations, but remains strong enough to

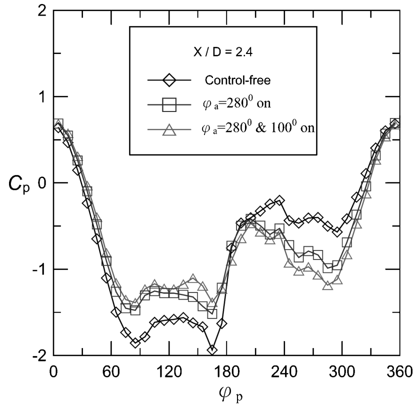

Fig. 17 Surface pressure distributions of cone–cylinder flows with and without control actuation: AOA = 55 deg and $\varphi_r = 70$ deg.

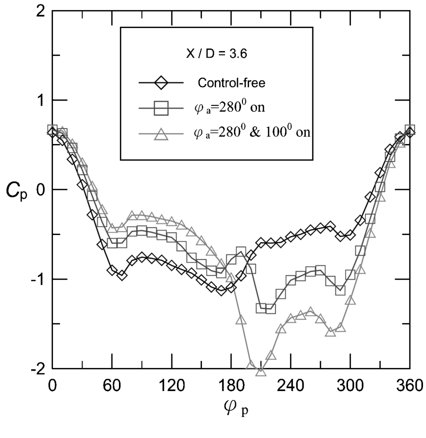

Fig. 18 Surface pressure distributions of cone–cylinder flows with and without control actuation: AOA = 55 deg and $\varphi_r = 70$ deg.

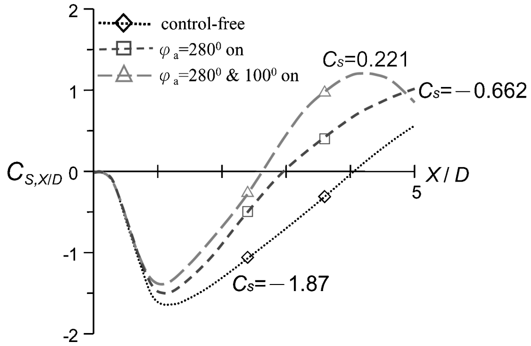

Fig. 19 Sectional side force $C_{s,X/D}$ distribution along body: AOA = 55 deg and $\varphi_r = 70$ deg; total side force coefficients equal to $C_s = -1.87$, $C_s = -0.662$, and $C_s = 0.221$ for control-free, single-actuation, and doube-actuation fowfields, respectively.

change the direction of the side force. Nevertheless, farther downstream, the asymmetric surface pressure distribution at the cross section $X/D = 3.6$ (Fig. 18) clearly switches the direction of the sectional side force as control actuations are activated.

By integration of surface pressure C_p distributions in Figs. 17 and 18, the sectional side force coefficients $C_{s,X/D}$ at location X/D for control-free and control-on cases are shown in Fig. 19. Though there are only two sectional side forces ($X/D = 2.4$ and 3.6) available, three schematic lines showing the sectional side force distributions developed along the body, for control-free and control-on cases, are shown in Fig. 19 based on the following evidence:

1) In accordance with the studies by Lamont and Hunt,[1] the side force distribution of an ogive–cylinder was found to be oscillatory along the slender body. Though Lamont and Hunt's[1] model is different from the current cone–cylinder, the high-AOA characteristics between an ogive–cylinder and a cone–cylinder differ only in onset angles and magnitude of side force. The sectional side force distributions of cone–cylinder slender body, therefore, should have similar oscillatory behavior along the slender body.

2) The sectional side forces show a trend of increase from a smaller (or negative) value at $X/D = 2.4$ to a larger (or positive) value at $X/D = 3.6$. This indicates a significant side force variation occurring along the slender body.

3) The total side forces vary from $C_s = -1.78$ for the control-free case to $C_s = 0.221$ for the double-actuation case. This suggests that the sectional side force distributions appearing in Fig. 19 are mostly negative before microballoon actuation, and are then change to a mixed, partially negative and positive distribution as microballoon actuations are employed.

This fundamental trend change explains again the effect of the control-induced third vortex structure that produces additional suction pressure and the resultant counteracting side force as well. The total side force of the cone–cylinder can be changed from a significantly negative value ($C_s = -1.87$, control free) to a slightly positive value ($C_s = 0.221$, double actuation) using the present balloon-type flow control method. With microballoon actuation, the vortical structure on the weak vortex side undergoes dramatic change. The sectional side force changes in such a way that the positive and the negative parts of the distribution cancel each other, resulting in a large reduction of the net total side force.

VII. Conclusions

In this work, the reduction of side force via microballoon array actuation on a high-AOA cone–cylinder slender body was examined. A microballoon array actuator is formed using PDMS elastomer and micromolding techniques that can be packaged on curved surfaces of a cone–cylinder slender body. When controls are activated, the microballoon actuator can be inflated to a vertical height of about 1.2 mm, which exceeds the thickness of the attached boundary layer before separation.

In the search for the optimal side force control of a cone–cylinder slender body, aerodynamic force measurement experiments investigated the reduction of side force when employing a single or multi-actuator. Side force measurement results indicate that the effectiveness of microballoon actuation varies with the forcing locations. The side force can be effectively reduced provided a single actuator is placed on the weak vortex side, with a forcing angle range of $50 \sim 90$ deg, as measured from the windward stagnation line. For multi-actuator forcing, a simple rule was identified for the side force control strategy. The side force can be almost completely eliminated when the weak and strong side actuators are located oppositely in the effective forcing range of $50 \sim 90$ deg as measured from the windward stagnation line. The experimental results also show that, in the range $0 < \text{AOA} < 60$ deg, this control method can effectively alleviate the side force acting on the cone–cylinder for any roll angles.

The side force reduction mechanism was examined by surveying the surface pressure and velocity field measurements. Interestingly, rather than changing vortical flow structures from asymmetric to symmetric, as is often done by conventional control methods, the present microballoon array actuator control can increase the asymmetry of vortical structures. The reduction of side force can be characterized based on two major mechanisms. The first mechanism derives from the early weak-side vortex liftoff after microballoon actuation, causing a substantial change of the vortical structures. This mechanism enables the premature formation of a new (third) vortex originating upstream from a concentrated high vorticity in the near-wall region. The second mechanism involves the induced new (third) vortex being strengthened due to microballoon actuation. Because of the participation of the new (third) vortex that grows and lifts off from the weak vortex side of the slender body, the original vortex induction mechanism is altered, producing an oscillatory distribution of the sectional side force distribution along the body. In summary, microballoon actuators can enhance the evolution and growth of this newly generated near-wall (third) vortex structure. The control-induced mixed positive and negative parts of the sectional side forces can be manipulated to cancel one another out, thus, significantly reducing the total side force acting on the slender body at high AOA.

Acknowledgment

The authors would like to thank the National Defense Fund of the Republic of China, Taiwan, for financially supporting this research under Contract B91-542.

References

[1] Lamont, P. J., and Hunt, B. L., "Prediction of Aerodynamic Out-of-Plane Forces on Ogive-Nosed Circular Cylinder," *Journal of Spacecraft and Rockets*, Vol. 14, No. 1, 1977, pp. 38–44.

[2] Degani, D., and Levy, Y., "Asymmetric Turbulent Vortical Flows over Slender Bodies," *AIAA Journal*, Vol. 30, No. 9, 1992, pp. 2267–2273.

[3] Ericsson, L. E., "Challenges in High-Alpha Vehicle Dynamics," *Progress in Aerospace Sciences*, Vol. 31, No. 4, 1995, pp. 291–334.

[4] Liu, P., and Deng, X., "Experimental Investigation of Aerodynamic Characteristics on Slender Bodies at High Angles of Attack," *Canadian Aeronautics and Space Journal*, Vol. 49, No. 1, 2003, pp. 31–40.

[5] Zilliac, G. G., Degani, D., and Tobak, M., "Asymmetric Vortices on a Slender Body of Revolution," *AIAA Journal*, Vol. 29, No. 5, 1991, pp. 667–675.

[6] Luo, S. C., Lim, T. T., Lua, K. B., and Chia, H. T., "Flowfield Around Ogive/Elliptic-Tip Cylinder at High Angle of Attack," *AIAA Journal*, Vol. 36, No. 10, 1998, pp. 1778–1787.

[7] Pick, G. S., "Investigation of Side Forces on Ogive–Cylinder Bodies at High Angles of Attack in the $M = 0.5$ to 1.1 Range," AIAA Paper 71-0570, June 1971.

[8] Brandon, J. M., and Nguyen, L. T., "Experimental Study of Effect of Forebody Geometry on High Angle-of-Attack Stability," *Journal of Aircraft*, Vol. 25, No. 7, 1988, pp. 591–597.

[9] Moskovitiz, C. A., Hall, R. M., and DeJarnette, F. R., "Effects of Nose Bluntness, Roughness and Surface Perturbations on the Asymmetric Flow Past Slender Bodies at Large Angles of Attack," AIAA Paper 89-2236, Aug. 1989.

[10] Luo, S. C., Lua, K. B., and Goh, E. K. R., "Side Force on an Ogive Cylinder: Effects of Surface Roughness," *Journal of Aircraft*, Vol. 39, No. 4, 2002, pp. 716–718.

[11] Rao, D. M., “Side-Force Alleviation on Slender, Pointed Forebodies at High Angles of Attack,” *Journal of Aircraft*, Vol. 16, No. 11, 1979, pp. 763–768.

[12] Clark, W. H., and Peoples, J. R., “Occurrence and Inhibition of Large Yawing Moments During High-Incidence Flight of Slender Missile Configurations,” *Journal of Spacecraft*, Vol. 10, No. 8, 1973, pp. 510–519.

[13] Asghar, A., Stahl, W. H., and Mahmood, M., “Suppression of Vortex Asymmetry and Side Force on a Circular Cone,” *AIAA Journal*, Vol. 32, No. 10, 1994, pp. 2117–2120.

[14] Moskovitz, C. A., Hall, R. M., and DeJarnette, F. R., “New Device for Controlling Asymmetric Flowfields on Forebodies at Large Alpha,” *Journal of Aircraft*, Vol. 28, No. 7, 1991, pp. 456–462.

[15] Fidler, J. E., “Active Control Asymmetric Vortex Effects,” *Journal of Aircraft*, Vol. 18, No. 4, 1981, pp. 267–272.

[16] Gittner, N. M., and Chokani, N., “Effects of Nozzle Exit Geometry of Forebody Vortex Control Using Blowing,” *Journal of Aircraft*, Vol. 31, No. 3, 1994, pp. 503–509.

[17] Hodgkin, F., and Wood, N. J., “Forebody Flow Control for Extended High-Angle-of-Attack Maneuvers,” *Journal of Aircraft*, Vol. 35, No. 2, 1998, pp. 212–217.

[18] Pedreiro, N., Rock, S. M., Celik, Z. Z., and Roberts, L., “Row-Yaw Control at High Angle by Forebody Tangential Blowing,” *Journal of Aircraft*, Vol. 35, No. 1, 1998, pp. 69–77.

[19] Roos, F. W., “Microblowing for High-Angle-of-Attack Vortex Flow Control on a Fighter Aircraft,” *Journal of Aircraft*, Vol. 38, No. 3, 2001, pp. 454–457.

[20] Rao, D. M., and Campbell, J. F., “Vortical Flow Management Techniques,” *Progress in Aerospace Sciences*, Vol. 24, No. 3, 1987, pp. 173–224.

[21] Malcolm, G. N., “Forebody Vortex Control,” *Progress in Aerospace Sciences*, Vol. 28, No. 3, 1991, pp. 171–234.

[22] Srivastava, B., “Computational Analysis and Validation for Lateral Jet Controlled Missiles,” *Journal of Spacecraft and Rockets*, Vol. 34, No. 5, 1997, pp. 584–592.

[23] Kikumoto, K., Sentoh, E., Tanaka, H., and Takahashi, T., “Sidejet Aerodynamic Interaction Effects of the Missile,” *AIAA Journal*, Vol. 39, No. 4, 2001, pp. 611–617.

[24] Grosjean, C., Lee, G. B., Hong, W., Tai, Y. C., and Ho, C. M., “Micro Balloon Actuators for Aerodynamic Control,” *IEEE MEMS-98 Workshop*, IEEE Publications, Piscataway, NJ, 1998, pp. 166–171.

[25] Lee, G. B., Shih, C., Liu, C., Huang, A., and Ho, C. M., “Robust Vortex Control of a Delta Wing by Distributed Microelectromechanical-System Actuators,” *Journal of Aircraft*, Vol. 37, No. 4, 2000, pp. 697–706.

[26] Huang, C. F., Silva, C., Christensen, B., Chen, Y., Ho, C. M., Jiang, F., Grosjean, C., Tai, Y. C., Lee, G. B., Chen, M., and Newbern, S., “Application of MEMS Devices to Delta Wing Aircraft: From Concept Development to Transonic Flight Test,” AIAA Paper 2001-0124, Jan. 2001.

[27] Chang, J. R., “Application of Micro Balloon Actuator on Forebody Aerodynamic Control,” Ph.D. Dissertation, Dept. of Aeronautics and Astronautics, National Cheng Kung Univ., Tainan, Taiwan, ROC, 2004.

[28] Khoo, M., and Liu, C., “Micro Magnetic Silicone Elastomer Membrane Actuator,” *Sensors and Actuators A*, Vol. 89, No. 3, 2001, pp. 259–266.